Biointerface Research in Applied Chemistry
Open-Access Journal (ISSN: 2069-5837)

Article
Volume 13, Issue 4, 2023, 390
https://doi.org/10.33263/BRIAC134.390

Synthesis and Characterization of Heat-Tempered $Cu_2Zn_{0.6}Ca_{0.4}SnS_4$ Alloy Thin Film

Olusola Akinrinola [1,*], Mojoyinola Kofoworola Awodele [1], Abideen A. Ibiyemi [2], Olusesan Abel Olu-Arotiowa [3], Omowunmi Abidemi Akinrinola [1], George Atilade Alagbe [1], Ayodeji Oladiran Awodugba [1]

[1] Department of Pure and Applied Physics, Faculty of Pure and Applied Sciences, Ladoke Akintola University of Technology, Ogbomoso, Nigeria; oakinrinola40@lautech.edu.ng (O.A.), mkawodele@lautech.edu.ng (M.K.A.), omowunmiabidemi.akinrinola@gmail.com (O.A.A.), gaalagbe@lautech.edu.ng (G.A.A.), aoawodugba@lautech.edu.ng (A.O.A.);,
[2] Department of Physics, Federal University Oye-Ekiti, Oye-Ekiti, Nigeria; abideen.ibiyemi@fuoye.edu.ng (A.A.I.);
[3] Department of Chemical Engineering, Faculty of Engineering and Technology, Ladoke Akintola University of Technology, Ogbomoso, Nigeria; oaolu-arotiowa@lautech.edu.ng (O.A.O.-A.);
* Correspondence: oakinrinola40@lautech.edu.ng (O.A.);

Scopus Author ID 57195735050
Received: 27.06.2022; Accepted: 17.07.2022; Published: 31.10.2022

Abstract: Six samples of $Cu_2Zn_{0.6}Ca_{0.4}SnS_4$ labeled $Y_1 - Y_6$ were spin-coated on a pre-cleaned glass from 20 ml each of 0.067 moll Calcium sulfate ($CaSO_4$, 98.5% Kermer^R) and 0.1 mol each of zinc nitrate ($Zn(NO_3)_2$, 99% Aldrich), Copper(II)sulfate hexahydrate ($Cu_2SO_4.6H_2O$, 98.5% Kermer^R), stannous sulfate ($SnSO_4$, 99% Kermer^R), and sodium thiosulfate ($Na_2S_2O_3$, 98.5% Aldrich) with ammonium hydroxide (NH_4OH, 99% DHR) and triethanolamine ($C_6H_{15}NO_3$, 99% Kermer^R) used as complexing agents. They were left to dry at room temperature. $Y_2 - Y_6$ were subjected to heat tempering in a carbolite furnace between 150 - 750 °C with a step height of 150 °C. The alloy thin films were structurally, morphologically, and optically characterized. The grain sizes for Y_1, Y_2, Y_3, Y_4, Y_5, and Y_6 are 15 nm, 40nm,43 nm, 45 nm, 44 nm, and 42 nm, respectively. The interruption of the normal stacking sequence of atomic planes initially decreases as the temperature increases and the microstrain. The microstrain and stacking fault energy both climaxed at 600 °C. Microstrain and stacking fault energy exhibit a sine and allometric relationship with the temperature (T). As the temperature increases, the band gap reduces from 3.60 eV to 3.26 eV. The residue effect of heat on the band gap variation gives a relative exponential decay of the crystallite. The difference between a shift in energy and a change in optical band gap (ΔE_{strain}) as a function of temperature is given as $-0.031 \pm 3.66667 \times 10^{-4}T$.

Keywords: alloy; thin films; optical band gap; shift in energy; microstrain.

1. Introduction

Cu_2ZnSnS_4 (CZTS) is a four-element alloy semiconducting material that has sparked interest in thin-film solar cells since the late 2000s [1]. Other A_2-B-D-F_4 (where A, B, D, and F are groups:1,2,4, and 6 of the periodic table) materials include Cu, Zn, Sn, and Se (CZTSe), and the S-Se alloy CZTSSe. CZTS has optical and electronic properties similar to CIGS (Cu, In, Ga, and Se) [2,3]. It is researched to be an intrinsic p-type, high absorption coefficient and direct optical band gap of around 1.6 eV, thus making it a good choice for a thin-film solar cell absorber layer [4,5]. The irregularity of the Cu-Zn cations makes it challenging to determine

the material's structure. It is the most prevalent defect that may be anticipated by theoretical analysis and verified by spectroscopy techniques [6].

The architecture may be misidentified due to the complex arrangement of the copper and zinc atoms. According to the theoretical analysis result, the instability of the Cu-Zn cations is expected to create unnecessary variations within the CZTS thin-film alloy [7]. As a result, this random ordering causes the materials within the solar cell to have the potential to generate a significant open circuit deficit which is the primary limiting factor for contemporary solar cell devices [8-10].

However, reducing or eliminating the disorder can be done by [11,12] elemental substitution through heterogeneous phase and temperature treatments. Here, $Cu_2Zn_{0.6}Ca_{0.4}SnS_4$ (CZCTS) is synthesized and heat tempered. We investigate the effect of heat tempering on the alloy thin film prepared through the chemical precipitation route and spin-coating technique by considering its crystallographic structures, surface morphology, optical properties, and I-V characteristics [13].

2. Materials and Methods

2.1 Synthesis of nanocrystal thin film.

CZCTS nanocrystals were synthesized in a beaker containing 20 ml each of 0.067 mol of Calcium sulfate ($CaSO_4$, 98.5% Kermer^R) and 0.1 mol each of zinc nitrate ($Zn(NO_3)_2$, 99% Aldrich), Copper(II)sulfate hexahydrate ($Cu_2SO_4.6H_2O$, 98.5% Kermer^R), stannous sulfate ($SnSO_4$, 99% Kermer^R), and sodium thiosulfate ($Na_2S_2O_3$, 98.5% Aldrich) with ammonium hydroxide (NH_4OH, 99% DHR) and triethanolamine ($C_6H_{15}NO_3$, 99% Kermer^R) used as complexing agents. The mixture was heated for 90 minutes at 90 °C while stirring. 50 ml of ethanol was added to it after cooling and was centrifuged at 5000 rpm for [14] 20 minutes to let the crystal flocculate and precipitate to remove unreacted chemicals for the first time. Two times afterward, 50 ml of deionized was added each time it was centrifuged; each set took 20 minutes.

The final residue was air dry. 0.1 gram of the air-dry crystals were dispersed in distilled water to form a homogenous solution and spin-coated on a soda-lime glass at 3000 rpm for 30 sec to create a 35 nm thin film. The spin-coated thin film (six in number) was allowed to dry at room temperature. Five spin-coated thin films were heat-tempered by a carbolite furnace in the range of 150 - 750 °C with a step height of 150 °C and were named Y_2 – Y_6 and Y_1 for reference samples without heat tempering. All the materials were optically, morphologically, and structurally characterized.

2.2. Characterization techniques.

The crystallographic data were acquired by using diffraction (XRD) on the alloy thin film. Measurements were made using CuK α radiation with a wavelength of 0.154 nm to obtain the XRD patterns of the CZTS nanostructures [11] for; Y_1, Y_2, Y_3, Y_4, Y_5, and Y_6 (Rigaku mini flex 600). The crystals' surface nano-morphology was obtained from a scanning electron microscope (Phenom prox). The elemental composition was done by energy-dispersive x-ray (EDX). Optical characterization [11,15] was evaluated by a UV-Vis-IR spectrometer (AvaSpec 3648). The effects of temperature on the crystallite size, microstrain, and stacking fault' [16-19] regarding the temperature change were also evaluated using Equations 2.1 to 2.5 [17-22];

$$\tau = \frac{k\lambda}{\beta \cos\theta} \tag{2.1}$$

where τ is the mean size of the ordered crystalline domain, k is the dimensionless shape factor known as Scherrer's constant with a value of 0.9 [17], and β is the line broadening at half the maximum intensity (FWHM) (rad), and θ is the Bragg [17,18] diffraction angle.

$$\frac{1}{d^2} = [h^2 + k^2 + l^2]\left[\frac{1}{a^2}\right] \tag{2.2}$$

$$\delta = \frac{1}{D^2} \tag{2.3}$$

$$SF = \left[\frac{2\Pi^2}{45(3\tan\theta)^{\frac{1}{2}}}\right] \tag{2.4}$$

$$\varepsilon = \frac{\beta \cos\theta}{4} \tag{2.5}$$

where a is the lattice constants, (h, k, l) are the miller indices, D is the grain size, and d [22-29] is the inter-planar spacing.

3. Results and Discussion

The XRD spectra of the six samples at varying temperatures are revealed. The effect of tempering on the thin-film samples is presented in Figure 1 [28-30]. The diffraction pattern obtained from the XRD exhibited a polycrystalline nature. It is revealed here that some diffraction peaks appear as the temperature increases until 600 °C, but these peaks resurface at 750 °C. The cliffs that appear are; (100), (210), (220), (410), (421), and (522) at. All these peaks were not present until the samples were heat treated. The grain sizes for Y_1, Y_2, Y_3, Y_4, Y_5, and Y_6 are 15 nm, 40nm,43 nm, 45 nm, 44 nm, and 42 nm, respectively. The grain size increases as the temperature increases, but the size expands towards 600 °C and eventually shrinks afterward.

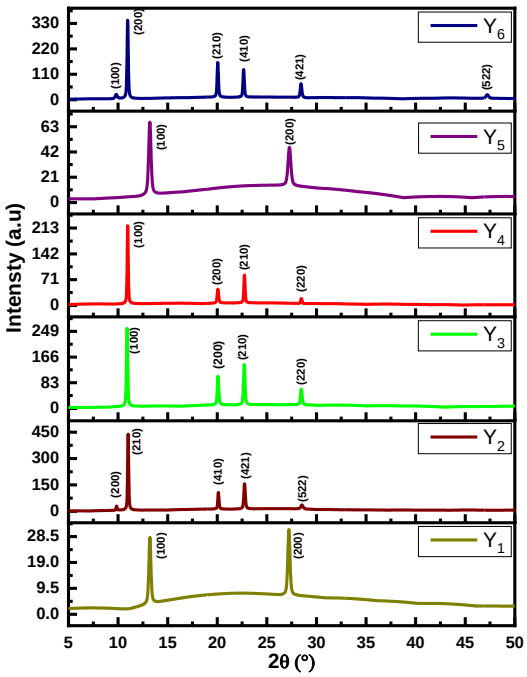

Figure 1. XRD patterns of CZCTS thin films for Y_1, Y_2, Y_3, Y_4, Y_5, and Y_6 as subjected to different temperatures.

The initial increase in length may be due to the aggregation of grains that later broke as the temperature approached 600 °C. It may be due to the assembly of many crystallites forming these grains. The same will be accounted for in the behavior of the dislocation density since it is inversely proportional to the square of the grain size observed in SEM micrographs, as shown in Figure 2. The Williamson-Hall (W-H) method was used to estimate the intrinsic strain and crystal size of the alloy thin films from the XRD profiling [11,31], as stated in Equation 2.1 and presented in Table 1.

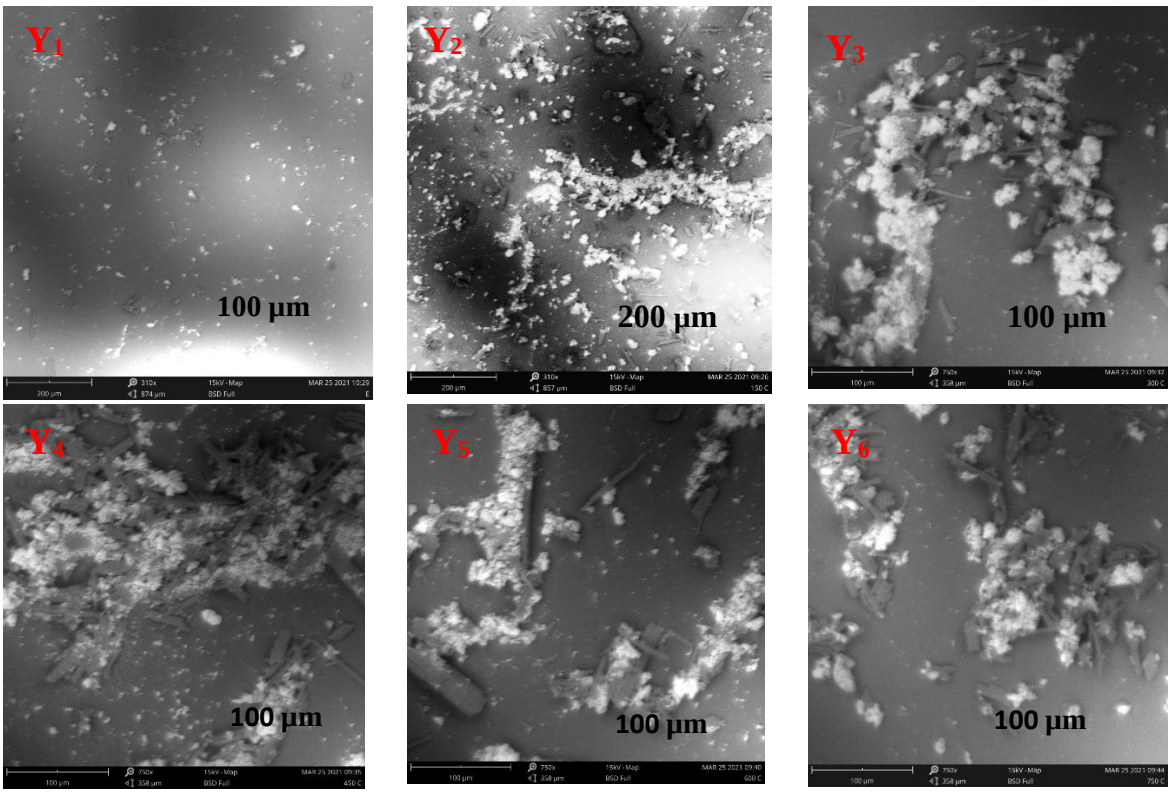

Figure 2. Scanning electron microscopy images of Y_1, Y_2, Y_3, Y_4, Y_5, and Y_6. Alloy thin films.

Table 1. The microstrain, stacking fault energy, crystal size, and optical band gap for the samples; Y_1, Y_2, Y_3, Y_4, Y_5, and Y_6.

Samples	Microstrain (µm/m)	Stacking fault	Crystal size	Band gap
Y_1	0.13014	0.63846	15.78320	3.60
Y_2	0.14192	0.66064	40.86000	3.51
Y_3	0.16427	0.68225	43.09335	3.47
Y_4	0.16657	0.69184	45.43093	3.41
Y_5	0.15709	0.71449	44.15758	3.35
Y_6	0.14401	0.68745	42.05508	3.26

Figure 3 illustrates the effect of heat on the alloy's microstrain (με) and stacking fault energy (γ_{SFE}). The interruption of the typical stacking sequence of atomic planes initially decreases as the temperature increases and the microstrain. The microstrain and stacking fault energy both climaxed at 600 °C. Microstrain and stacking fault energy exhibit a sine and allometric relationship with the temperature (T), and the models for both (με) and (γ_{SFE}) for the materials are presented in Equations 3.1 and 3.2, respectively.

$$\mu\varepsilon = (0.14521 \pm 0.00929) + (0.02219 \pm 0.00805)\sin\left[\frac{\pi(T-(158.82773 \pm 93.65109)}{(565.48424 \pm 176.31184)}\right] \quad (3.1)$$

$$\gamma_{SFE} = (0.58647 \pm 0.01455)T^{(0.02591 \pm 0.00436)} \quad (3.2)$$

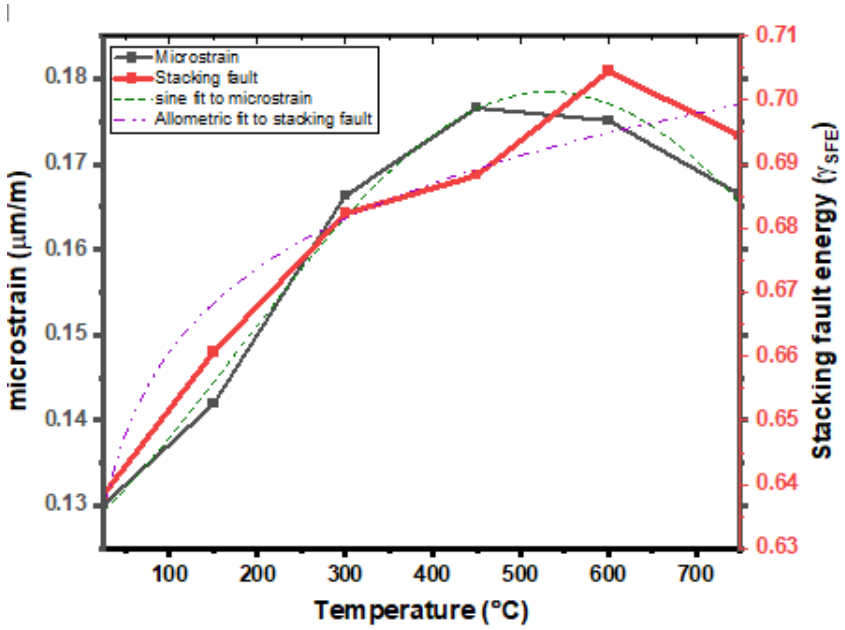

Figure 3. Microstrain and stacking fault energy of CZCTS thin film samples of Y_1, Y_2, Y_3, Y_4, Y_5, and Y_6. as a function of temperature with sine fit and allometric fit models for microstrain and stacking fault energy.

The optical transmittance, which is the effectiveness of the alloy in transmitting radiant energy, is presented after heat treatment. The shown plots illustrate the variation of optical transmittance of the alloy, which was annealed at 150 ℃ – 750 ℃ with a step height of 150 ℃, as shown in Figure 4. The alloy showed better transmittance performance with 450 ℃ and 600 ℃. The optical absorbance of the heat treatment of the alloy, $Cu_2Zn_{0.6}Ca_{0.4}SnS_4$, was obtained using a UV-VIS-IR spectrophotometer. Figure 5 depicts the variation in the alloy along with the wavelength and temperature. The alloy revealed excellent absorption as the temperature increased, showing a greater absorption at 600 ℃. The materials revealed the presence of direct optical band gaps. The band gap of the material is obtained through the absorption spectrum using a Tauc plot [23];

$$(\alpha h\nu)^n = \beta(h\nu - E_g) \quad (3.3)$$

where Eg is the material's band gap, h is the Planck constant, v if the frequency, β is as described in Equation 2.1[21], α is the absorption coefficient, and n can take a value of 2 for indirect band gap and 0.5 for direct band gap. The graph of $(\alpha h\nu)^n$ against hv for n, as the case may be for the direct band gaps revealed in Figure 6. As the temperature increases, the band gap reduces from 3.60 eV to 3.26 eV (Table 1). Figure 7 shows the variation of the band gap of the thin film with the crystallite size [11,29,30]. It shows that the residue effect on the difference in the band gap [31-33] gives a relative exponential decay on the crystallite size (D). The exponential relationship from the plot is presented as Equation 3.4.

$$E_g = -4.95914 * 10^{-8} e^{\frac{-D}{-2.90805}} - 4.95914 * 10^{-8} e^{\frac{-D}{-3.23117}} + \left(-4.95914 * 10^{-8} e^{\frac{-D}{-3.55429}} + 3.60002\right) \quad (3.4)$$

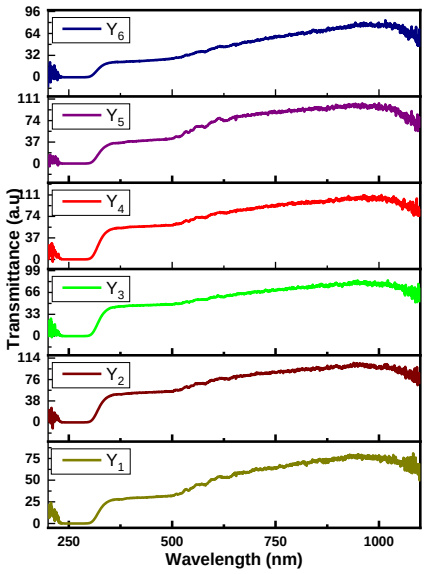

Figure 4. Transmittance spectrum of CZCTS thin film samples for Y_1, Y_2, Y_3, Y_4, Y_5, and Y_6.

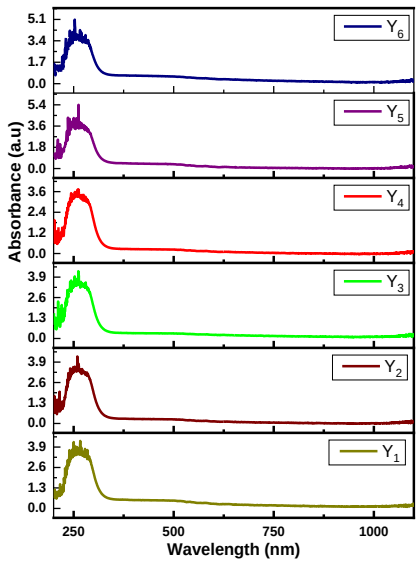

Figure 5. Absorption spectrum of CZCTS thin film samples for Y_1, Y_2, Y_3, Y_4, Y_5, and Y_6.

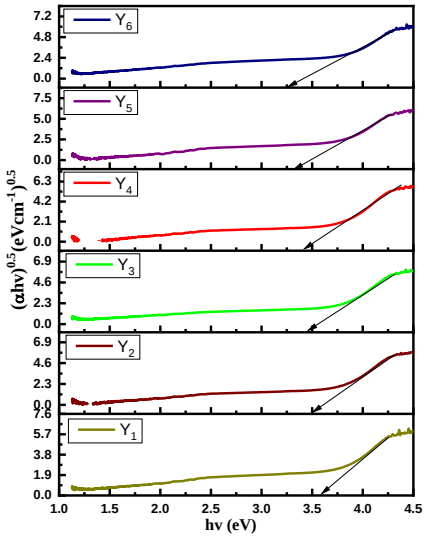

Figure 6. Band gap plots of CZCTS thin film samples for Y_1, Y_2, Y_3, Y_4, Y_5, and Y_6.

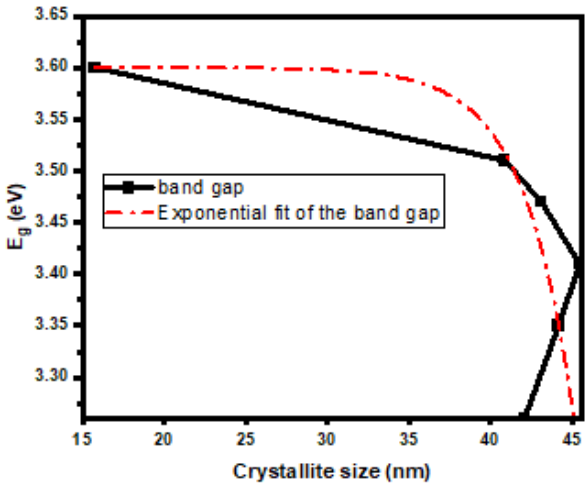

Figure 7. Variation of band gap with crystallite size for thin film samples (Y_1, Y_2, Y_3, Y_4, Y_5, and Y_6.) and exponential fit of the band gap model.

The upward change in temperature has caused the material's energy band gap reduction. This red change within the optical band gap of the material is due to the forceful quantum confinement of more electrons in the conduction band [11, 27,28]. We also observed that the intrinsic strain varies according to the crystal size and crystallinity of the materials, as presented in Table 2.

Table 2. The crystallinity, band gap shift energy, the shift in the bulk optical band gap, and change in strain for the samples; Y_1, Y_2, Y_3, Y_4, Y_5, and Y_6.

ITEMS	Y_1	Y_2	Y_3	Y_4	Y_5	Y_6
Crystallinity (%)	83.12	87.29	92.85	90.46	90.12	88.45
ΔE_{SE}	-	0.11	0.13	0.19	0.25	0.34
ΔE_g	-	0.09	0.04	0.06	0.07	0.09
ΔE_{strain}	-	0.02	0.09	0.13	0.18	0.25

It has been reported that strain is often responsible for the change "of the optical band gap." Therefore the optical band gap decrease can be attributed to the change in size effect and intrinsic strain caused by the increase in temperature. It is attributed to the relative contribution of these factors to the reduction in the bandgaps vis a vis the crystal size and upward change in temperature. In the weak confinement region, the shift in the energy band gap (ΔE_{SE}) is expressed as [11];

$$\Delta E_{SE} = \frac{\pi^2 \hbar^2}{2R^2}\left\{\frac{1}{m_e^*} + \frac{1}{m_h^*}\right\} - \frac{18e^2}{40\pi\varepsilon_o\varepsilon R}$$

$$\Delta E_{SE} = E_B - E_g \quad (3.5)$$

where R is the particle's radius, m_e^* and m_h^* are the effective masses of electron and hole, respectively, ε_o is the dielectric constant of free space, ε is the dielectric constant of CZCTS (approximately 8.5), e is the electronic charge, E_g and E_B are the energy band gaps for the material and its bulk respectively. The change in optical band gap due to temperature is given as follows;

$$\Delta E_g = E_{g1} - E_{g2} \quad (3.6)$$

where ΔE_g is the change in the optical band gap between two marked temperature step heights, E_{g1} is the initial band gap at the initial temperature, and E_{g2} is the final temperature at that instance. The plot of the shift in energy band gap with temperature variation is thus given in Figure 8. The contribution of the strain in the band gap of the CZCTS thin film is shown in Table 1. Also, the contribution of ΔE_{strain} of the CZCTS thin film can be estimated with Equation 3.7 as;

$$\Delta E_{strain} = \Delta E_{SE} - \Delta E_g \quad (3.7)$$

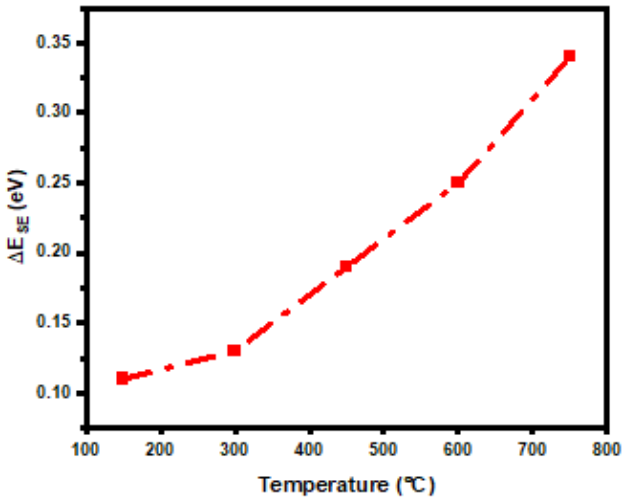

Figure 8. Variation of the shift in energy band gap versus temperature in the samples (Y_1, Y_2, Y_3, Y_4, Y_5, and Y_6).

Figure 9 shows the variation of ΔE_{strain} in the temperature of the CZCTS thin film. Thus to get the idea of the dependence of the ΔE_{strain} on the bulk thin film as related to temperature, the model derived from the plot is given as Equation 3.8.

$$\Delta E_{strain} = -0.031 \pm 3.66667 \times 10^{-4} T \quad (3.8)$$

It clearly shows that the observed decrease in the bandgap with increased crystallite was due to the induced intrinsic strain by the increase in temperature of the thin films.

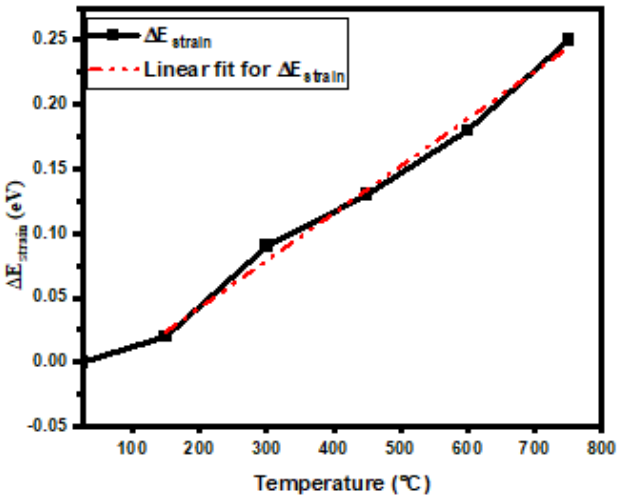

Figure 9. Variation of the intrinsic strain versus temperature with the linear fit of the inherent strain model for the thin film.

4. Conclusions

We have successfully studied the residue effect of heat on the CZCTS thin film at varying temperatures. XRD revealed new peaks which are initially absent in the bulk thin film. The intrinsic strain must have induced these new peaks. When the temperature rises, the grain size increases but decreases as it reaches 600°C. It is thus possible that the initial growth was caused by grains clumping together and breaking apart when the temperature hit 600 °C. Many crystallites may have aggregated to make these grains, which might explain it. As the alloy's temperature rose, it showed more absorption, peaking at 600 degrees Celsius. Direct optical band gaps were found in the materials. The effect of temperature on the impact of the band gap fluctuation generates a relative exponential decrease in the crystallite size, according to the study results. As a result, the shrinkage of the optical band gap may be linked to temperature-induced changes in the size effect and intrinsic strain. The relative influence of these variables on the decrease in the band gaps concerning crystal size and upward temperature change is thus confirmed.

Funding

This research received no external funding.

Acknowledgments

We declare no acknowledgment.

Conflicts of Interest

The authors declare no conflict of interest.

References

1. Khemiri, N.; Chamekh, S.; Kanzari, M. Properties of thermally evaporated CZTS thin films and numerical simulation of earth-abundant and non-toxic CZTS/Zn(S, O) based solar cells. *Solar Energy* **2020,** *207*, 496–502, https://doi.org/10.1016/j.solener.2020.06.114.

2. Kumar, M.; Dubey, A.; Adhikari, N.; Venkatesan, S.; Qiao, Q. Strategic review of secondary phases, defects and defect-complexes in kesterite CZTS–Se solar cells. *Energy & Environmental Science* **2015,** *8*, 3134-3159, https://doi.org/10.1039/C5EE02153G.
3. Li, Y.; Chen, J.; Ma, J. Properties of Cu_2ZnSnS_4 (CZTS) thin films prepared by plasma-assisted co-evaporation. *Journal of Materials Science: Materials in Electronics* **2015,** *26*, 6546-6551, https://doi.org/10.1007/s10854-015-3251-5.
4. Abd El Halim, B.; Mahfoud, A.; Elamine, D.M. Numerical analysis of potential buffer layer for Cu_2ZnSnS_4 (CZTS) solar cells. *Optik* **2020,** *204*, 164155, https://doi.org/10.1016/j.ijleo.2019.164155.
5. Min, H.S.; Hardani, C.; Supriyanto, A. Thin Film-Based Solar Cell and Dye-Sensitized Solar Cells: Review. *International Journal of Advanced Science and Technology* **2020,** *29*, 2413-2426.
6. Morales, M.P.; Pecharroman, C.; Carreñ, T.G.; Serna, C. J. Structural characteristics of uniform γ-Fe_2O_3 particles with different axial (length/width) ratios. *Journal of Solid State Chemistry*, **1994,** *108*, 158-163, https://doi.org/10.1006/jssc.1994.1024.
7. Lafond, A.; Guillot-Deudon, C.; Vidal, J.; Paris, M.; La, C.; Jobic, S. Substitution of Li for Cu in Cu_2ZnSnS_4: toward wide band gap absorbers with low cation disorder for thin film solar cells. *Inorganic Chemistry* **2017,** *56*, 2712-2721, https://doi.org/10.1021/acs.inorgchem.6b02865.
8. Hadke, S.; Chen, W.; Tan, J.M.R.; Guc, M.; Izquierdo-Roca, V.; Rignanese, G. M., Wong, L.H. Effect of Cd on cation redistribution and order-disorder transition in $Cu_2(Zn,Cd)SnS_4$. *Journal of Materials Chemistry A* **2019,** *7*, 26927-26933, https://doi.org/10.1039/c9ta09572a.
9. Berthelot, R.; Schmidt, W.; Muir, S.; Eilertsen, J.; Etienne, L.; Sleight, A.W.; Subramanian, M.A. New layered compounds with honeycomb ordering: $Li_3Ni_2BiO_6$, Li_3NiM' BiO_6 (M′= Mg, Cu, Zn), and the delafossite $Ag_3Ni_2BiO_6$. *Inorganic chemistry* **2012,** *51*, 5377-5385, https://doi.org/10.1021/ic300351t.
10. Isotta, E.; Syafiq, U.; Ataollahi, N.; Chiappini, A.; Malerba, C.; Luong, S.; Scardi, P. Thermoelectric properties of CZTS thin films: Effect of Cu–Zn disorder. *Physical Chemistry Chemical Physics* **2021,** *23*, 13148-13158, https://doi.org/10.1039/D1CP01327K.
11. Ansari, M.Z.; Khare, N. Effect of intrinsic strain on the optical band gap of single phase nanostructured Cu_2ZnSnS_4. *Materials Science in Semiconductor Processing* **2017,** *63*, 220–226, https://doi.org/10.1016/j.mssp.2017.02.011.
12. Rudisch, K.; Davydova, A.; Platzer-Björkman, C.; Scragg, J. The effect of stoichiometry on Cu-Zn ordering kinetics in Cu_2ZnSnS_4 thin films. *Journal of Applied Physics* **2018** *123*, 161558, https://doi.org/10.1063/1.5010081.
13. Goswami, M.; Adhikary, N.C.; Bhattacharjee, S. Effect of annealing temperatures on the structural and optical properties of zinc oxide nanoparticles prepared by chemical precipitation method. *Optik* **2018**, *158*, 1006-1015, https://doi.org/10.1016/j.ijleo.2017.12.174.
14. Qiao, Z.; Yuan, Z.; Zhang, W.; Wei, D.; Hu, N. Preparation, in vitro release and antibacterial activity evaluation of rifampicin and moxifloxacin-loaded poly(D,L-lactide-co-glycolide) microspheres. *Artificial Cells, Nanomedicine, and Biotechnology* **2019,** *47*, 790–798, https://doi.org/10.1080/21691401.2019.1581792.
15. Ozmen, S. I.; Gubur, H.M. Synthesis and characterization of CdTe/CdSe thin film on glass/ITO by electrodeposition at room temperature. *Bulletin of Materials Science* **2022,** *45*, 1-8, https://doi.org/10.1007/s12034-021-02653-6.
16. Nagaraj, M.; Ravisankar, B. Effect of Severe Plastic Deformation on Microstructural and Mechanical Properties of Structural Steel IS2062. *Transactions of the Indian Institute of Metals* **2018,** *71*, 2315–2323, https://doi.org/10.1007/s12666-018-1363-3.
17. Karthikeyan, S.; Judia Magthalin, C.; Mahesh, M.; Anandan, C.; Sekaran, G. Synthesis of reactive iron impregnated nanoporous activated carbon and its application in anaerobic biological treatment to enhance biodegradability of ortho-phenylenediamine. *Journal of Chemical Technology & Biotechnology* **2014,** *90*, 1013–1026, https://doi.org/10.1002/jctb.4403.
18. Saffarzadeh-Matin, S.; Khandan, M.; Shalmashi, A. Iranian natural zeolite particle modification: Green synthesis, characterization, and oil spill remediation. *Journal of Particle Science & Technology* **2019,** *5*, 77-90, https://doi.org/10.22104/JPST.2019.3517.1146.
19. Suresh, R.; Ponnuswamy, V.; Mariappan, R. Effect of annealing temperature on the microstructural, optical and electrical properties of CeO_2 nanoparticles by chemical precipitation method. *Applied Surface Science* **2013,** *273*, 457–464, https://doi.org/10.1016/j.apsusc.2013.02.062.

20. Zhang, Q.; Sun, X.; Zheng, W.; Wan, Q.; Liu, M.; Liao, X.; Li, L. Band Gap Engineering toward Wavelength Tunable $CsPbBr_3$ Nanocrystals for Achieving Rec. 2020 Displays. *Chemistry of Materials* **2021,** *33*, 3575-3584, https://doi.org/10.1021/acs.chemmater.1c00145.
21. Basyooni, M.A.; Al-Dossari, M.; Zaki, S.E.; Eker, Y.R.; Yilmaz, M.; Shaban, M. Tuning the Metal–Insulator Transition Properties of VO_2 Thin Films with the Synergetic Combination of Oxygen Vacancies, Strain Engineering, and Tungsten Doping. *Nanomaterials* **2022,** *12*, 1470, https://doi.org/10.3390/nano12091470.
22. Dustgeer, M.R.; Asma, S.T.; Jilani, A.; Raza, K.; Hussain, S.Z.; Shakoor, M.B.; Darwesh, R. Synthesis and characterization of a novel single-phase sputtered Cu2O thin films: Structural, antibacterial activity and photocatalytic degradation of methylene blue. *Inorganic Chemistry Communications* **2021,** *128*, 108606, https://doi.org/10.1016/j.inoche.2021.108606.
23. Feng, Y.; Zhang, Z.; Zhao, K.; Lin, S.; Li, H.; Gao, X. Photocatalytic nitrogen fixation: Oxygen vacancy modified novel micro-nanosheet structure Bi2O2CO3 with band gap engineering. *Journal of Colloid and Interface Science* **2021,** *583*, 499-509, https://doi.org/10.1016/j.jcis.2020.09.089.
24. Yan, H.; Matsushita, Y.; Yamaura, K.; Tsujimoto, Y. $La_3Ga_3Ge_2S_3O_{10}$: An Ultraviolet Nonlinear Optical Oxysulfide Designed by Anion-Directed Band Gap Engineering. *Angewandte Chemie International Edition* **2021,** *60*, 26561-26565, https://doi.org/10.1002/anie.202112692.
25. Guo, X.; Liu, L.; Xiao, Y.; Qi, Y.; Duan, C.; Zhang, F. Band gap engineering of metal-organic frameworks for solar fuel productions. *Coordination Chemistry Reviews* **2021,** *435*, 213785, https://doi.org/10.1016/j.ccr.2021.213785.
26. Goktas, A.; Modanlı, S.; Tumbul, A.; Kilic, A. Facile synthesis and characterization of ZnO, ZnO: Co, and ZnO/ZnO: Co nano rod-like homojunction thin films: Role of crystallite/grain size and microstrain in photocatalytic performance. *Journal of Alloys and Compounds* **2022,** *893*, 162334, https://doi.org/10.1016/j.jallcom.2021.162334.
27. Son, S.Y.; Lee, G.; Wang, H.; Samson, S.; Wei, Q.; Zhu, Y.; You, W. Integrating charge mobility, stability and stretchability within conjugated polymer films for stretchable multifunctional sensors. *Nature Communications* **2022,** *13*, 1-11, https://doi.org/10.1038/s41467-022-30361-0.
28. Amole, S.; Awodele, M.K.; Adedokun, O.; Jain, M.; Awodugba, A.O. Sol-Gel Spin Coating Synthesis of TiO_2 Nanostructure and Its Optical Characterization. *Journal of Materials Science and Chemical Engineering* **2019,** *7*, 23–34, https://doi.org/10.4236/msce.2019.76003.
29. Schriber, E.A.; Paley, D.W.; Bolotovsky, R.; Rosenberg, D.J.; Sierra, R.G.; Aquila, A.; Hohman, J.N. Chemical crystallography by serial femtosecond X-ray diffraction. *Nature* **2022,** *601*, 360-365, https://doi.org/10.1038/s41586-021-04218-3.
30. Thakar, M.A.; Jha, S.S.; Phasinam, K.; Manne,R.; Qureshi, Y.; Babu, V.H. X ray diffraction (XRD) analysis and evaluation of antioxidant activity of copper oxide nanoparticles synthesized from leaf extract of Cissus vitiginea. *Materials Today: Proceedings* **2022,** *51*, 319-324, https://doi.org/10.1016/j.matpr.2021.05.410.
31. Ayachi, M.; Ayad, F.; Djelloul, A.; Benharrat, L.; Anas, S. Synthesis and Characterization of Ni-Doped ZnO Thin Films Prepared by Sol–Gel Spin-Coating Method. *Semiconductors* **2021,** *55*, 482-490, https://doi.org/10.1134/S1063782621050043.
32. Nath, D.; Singh, F.; Das, R. X-ray diffraction analysis by Williamson-Hall, Halder-Wagner and size-strain plot methods of CdSe nanoparticles-a comparative study. *Materials Chemistry and Physics* **2020,** *239*, 122021, https://doi.org/10.1016/j.matchemphys.2019.122021.
33. Yadav, S.K.; Uberuaga, B.P.; Nikl, M.; Jiang, C.; Stanek, C.R. Band-Gap and Band-Edge Engineering of Multicomponent Garnet Scintillators from First Principles. *Physical Review Applied* **2015,** *4*, https://doi.org/10.1103/physrevapplied.4.054012.